International Journal of Multiphase Flow 159 (2023) 104337

Contents lists available at ScienceDirect

International Journal of Multiphase Flow

journal homepage: www.elsevier.com/locate/ijmulflow

Air–water properties of unsteady breaking bore part 2: Void fraction and bubble statistics

Rui Shi [a,*], Davide Wüthrich [a,b], Hubert Chanson [a]

[a] School of Civil Engineering, The University of Queensland, St Lucia, Brisbane, 4067, QLD, Australia
[b] Department of Hydraulic Engineering, Delft University of Technology, Delft, 2600 GA, The Netherlands

ARTICLE INFO

Keywords:
Unsteady gas–liquid flow
Breaking bore
Dual-tip phase detection probe
Image processing
Void fraction
Bubble clustering
Bubble size spectrum

ABSTRACT

Continuing from the part 1 (Shi et al., 2022) this paper presents an experimental investigation of transient void fraction and bubble statistics in a highly turbulent breaking bore with $Fr_1 = 2.4$. The measurements were conducted using a combination of dual-tip phase-detection probes and an ultra-high-speed video camera. The enclosed bubble detection technique (EBDT) used the synchronised probe and camera signals to provide the contour of instantaneous void fraction in the bore roller. The ensemble-averaged void fraction was derived, and compared to analytical solutions of air diffusion models. The bubble statistics were characterised by the bubble clustering properties, pseudo bubble count rate and bubble size spectrum. The clustering data showed the non-random bubble grouping in the shear layer, and the bubble size distributions $N(r)$ followed a commonly adopted bubble break-up model: $N(r) \propto r^{-m}$, where r was the equivalent bubble radius in the present study. The comparison indicated that, in the breaking bore, its air diffusion process was similar to that in a stationary hydraulic jump, and the bubble break-up process was comparable to that in breaking waves.

1. Introduction

A breaking bore is a complex air–water flow phenomenon, associated with air entrainment, energy dissipation and unsteady propagation (Fig. 1). Several events can generate breaking bores, such as the increase in the non-linearity of the motion of breaking wave (Peregrine, 1983), sudden rise of water in estuary by the moon gravity (tidal bore) (Chanson, 2012) and dam-break-like waves (Stansby et al., 1998). During the bore propagation, some pseudo-periodic flow patterns are observed, as vortices emerging at the wave front, free-surface jets forming and plunging back to the surface. A quasi-steady flow analogy may be used to describe the breaking bore as the hydraulic jump in transition (Lighthill, 1978). The presence of bubbles is of significance for several physical processes, including the impact forces on hydraulic and coastal structures (Bullock et al., 2001; Wüthrich et al., 2018), dissipation of wave energy (Lamarre and Melville, 1994; Blenkinsopp and Chaplin, 2007) and exchange of heat, gases and marine aerosols from free-surface water (Merlivat and Memery, 1983; Veron, 2015).

The literature on the air–water characteristics of unsteady breaking bore is limited. The series of works by Leng and Chanson (2019a,b) is the main ones, providing the direct measurements of basic air–water flow properties (void fraction data, bubble chord time and total number of interfaces) using phase-detection probes in the breaking roller. The literature review may be extended to some featured works in other self-aerated surface breakers, with a number of experimental studies providing detailed void fraction measurements in breaking waves. Several studies generated 2D and 3D contour plots of time-dependent void fraction using intrusive probes, showing the 30% to 50% of potential energy dissipated from the breaking, 6.5% to 14% consumed by air entrainment and splash on the free surface (Rapp and Melville, 1990; Lamarre and Melville, 1991, 1994; Cox and Shin, 2003; Hoque and Aoki, 2005; Blenkinsopp and Chaplin, 2007; Mori and Kakuno, 2008). The turbulence dissipation was linked to the bubble size spectrum in breaking waves (Garrett et al., 2000; Deane and Stokes, 2002; Rojas and Loewen, 2007). These studies suggested the bubble radius (r) distribution following a power law as: $N(r) \propto r^{-m}$, for $m \in [2.5, 3.5]$. On the other hand, extensive works have been conducted for the air–water flow measurements in steady hydraulic jumps. Recent studies were able to quantify the air diffusion process (Chanson, 1995; Mossa and Tolve, 1998; Leandro et al., 2012), free-surface dynamics (Brocchini and Peregrine, 2001; Wang et al., 2015b), non-random bubble regrouping (Wang et al., 2015a; Witt et al., 2015) and air–water turbulence (Rodríguez-Rodríguez et al., 2011; Wang et al., 2014; Mortazavi et al., 2016).

This work is part of a comprehensive study assessing the air–water flow properties in breaking bore. In part 1 (Shi et al., 2022), three techniques were proposed to provide both Eulerian and Lagrangian

* Corresponding author.
E-mail address: rui.shi@uq.net.au (R. Shi).

https://doi.org/10.1016/j.ijmultiphaseflow.2022.104337
Received 22 September 2021; Received in revised form 29 July 2022; Accepted 29 November 2022
Available online 5 December 2022

Fig. 1. Photographs of a breaking bore at See/Selune River on 24/09/10 (Photograph H. Chanson). The bore propagated from right to left.

velocity measurements in the breaking bore roller. Further investigations on the experimental data enabled the quantification of the air–water flow dynamics in the breaking roller, thus motivating this research. Herein, a combination of intrusive phase-detection and non-intrusive image-based techniques was adopted. Section 2 introduces the experimental set-up and signal processing. The image-based and analytical void fraction profiles are shown in Section 4. The bubble characteristics are discussed in Section 5, followed by a conclusion in Section 6.

2. Experimental facility and instrumentation

The present paper adopted the same experimental dataset used for part 1. Thus, the experimental set-up and instrumentation are only briefly introduced herein. The rectangular channel of 19 m long and 0.7 wide had an initial steady flow with a discharge $Q = 0.01$ m^3/s (Fig. 2). A sudden closure of the Tainter gate at the downstream channel end induced a breaking bore propagating upstream. Intrusively, the air–water properties were measured using an array of three dual-tip phase-detection probes, synchronised to an ultra-high-speed camera. Each probe was equipped with two needle sensors with the longitudinal separation distance Δx. The phase-detection probe array included the centreline probe with $\Delta x = 0.0051$ m on the channel centreline, a sidewall probe with $\Delta x = 0.0071$ m at 0.005 m from the wall, and a reference probe with $\Delta x = 0$ next to the centreline probe. All probes were sampled at 100 kHz at 20 vertical locations, ranging from $z/d_1 = 0.82$ to 2.85. For each locations, 100 repetitions were conducted based on an extensive sensitivity analysis (Shi et al., 2021b).

The ultra-high-speed video camera (Phantom v2011) was operated with full HD resolution (1280 × 800 pixels) and 10,000 frame per second (fps). The camera required an intensive Light Emitting Diode (LED) array to lighten the flow. The probe sensors were aligned at $x = 8.5$ m, which was covered in the left side of the image plane. Three acoustic displacement meters (ADMs) were placed on the channel centreline, to characterise the flow conditions listed in Table 1, where d_1 and d_2 are the conjugate depths measured by ADM; U is the mean bore front celerity calculated from ADM data, as the ratio between sensor distance and travelling time; V_1 is the initial flow velocity; Re is the Reynolds number defined as $Re = d_1(V_1 + U)/\nu$; Fr is the bore Froude number, defined as $Fr_1 = (V_1 + U)/(\sqrt{g d_1})$.

The positive longitudinal direction x was consistent with the initial flow. The positive vertical direction z pointed upwards, with zero at channel bed. The positive transverse direction y was perpendicular to the sidewall, with the positive direction pointing towards the camera.

Table 1
A summary of flow conditions in the breaking bore.

Q (m^3/s)	d_1 (m)	d_2 (m)	U (m/s)	V_1 (m/s)	Re	Fr_1
0.1	0.084	0.245	0.51	1.71	2.3 ×10^5	2.4

3. Enclosed Bubble Detection Technique (EBDT)

3.1. Presentation

A review on the quantification of gas–liquid properties using image-based techniques is given herein, leading to the development of the enclosed bubble detection technique (EBDT). In gas–liquid flow, image-based techniques can be classified into the brightness thresholding (Maurus et al., 2002; Leandro et al., 2012; Gabriel et al., 2018; Leng and Chanson, 2019b) and bubble recognition algorithms (Rana et al., 2014; Fu and Liu, 2016a,b). The former establishes a proportional relationship between the brightness and void fraction data. However, errors can be caused by the intensive reflection from the bubble surface and non-uniform lighting. The latter was considered more physically meaningful by highlighting the shapes of bubble or bubbly clouds, thus motivating the development of EBDT. A review on some featured bubble recognition algorithms in literature is given in Table 2, with all algorithms having a same step "bubble segmentation". The bubble segmentation aims to highlight individual bubble and to separate overlapping bubbles in clusters. The Hough Transform method (Pei and Horng, 1995) was able to accurately identify bubbles with circular shapes, whereas for non-circular bubbles, the bubble segmentation was based upon the breakpoint method (Teh and Chin, 1989) and watershed method (Meyer and Beucher, 1990). Depending on the purposes of these studies, some algorithms were able to perform bubble reconstruction, restoring the missing part of individual bubble. The common method of the bubble reconstruction was to fit an ellipse using the extracting bubble outlines.

Based upon above review, a novel image-based technique, called the enclosed bubble detection technique (EBDT), was derived for gas–liquid flow with strong turbulence. In EBDT, the phase-detection probes

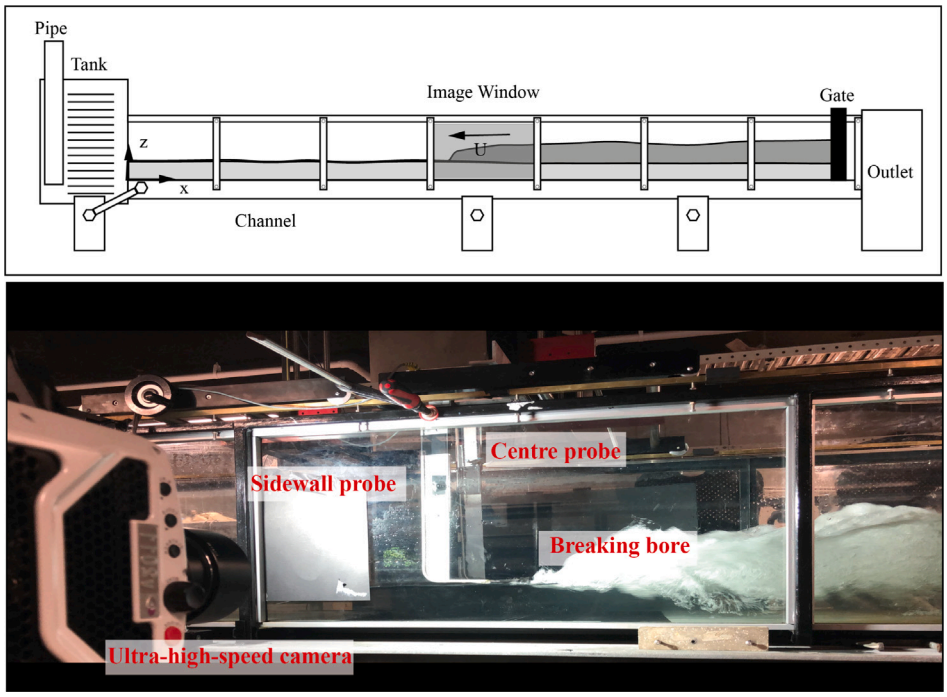

Fig. 2. Illustration of experimental set-up (Top) a sketch of experimental facility (Bottom) a photograph of instrumentation. Bore propagation from right to left.

Table 2
Review on bubble recognition algorithms in gas–liquid flow.

Reference	Void fraction	Bubble segmentation	Bubble reconstruction
Honkanen et al. (2005)	2%	Breakpoint	Ellipse fitting (more than 85% bubble outlines)
Bröder and Sommerfeld (2007)	5%	Sobel edge detection	Ellipse fitting
Yu et al. (2009)	N/A	Hough Transform	Ellipse fitting
Lau et al. (2013)	11%	Watershed	N/A
Rana et al. (2014)	15%	Roberts edge detection	N/A
Fu and Liu (2016a,b)	11%	Breakpoint & Watershed	Ellipse fitting
Chalgeri and Jeong (2019)	N/A	Watershed	N/A
Kong et al. (2019)	N/A	Moore-Neighbour tracing algorithm	N/A
Villegas et al. (2019)	9.33%	Watershed	Ellipse fitting
Poletaev et al. (2020)	2.5%	Convolutional neural networks	Ellipse fitting
Cerqueira and Paladino (2021)	1.41–9.03%	Convolutional neural networks	Ellipse fitting

were used for validation and synchronisation. The raw signal of phase-detection probes was in the form of voltage, with each voltage drop corresponding to a detection of an air bubble. The single threshold technique (Cartellier and Achard, 1991) was used to translate the raw signal to instantaneous void fraction signal $c(t)$, using a constant threshold of 50%:

$$\frac{S_{L\,or\,T}-\overline{Vo_a}}{\overline{Vo_w}-\overline{Vo_a}}\begin{cases}\geq 0.5 \Rightarrow c(t)=1 & \text{air}\\ <0.5 \Rightarrow c(t)=0 & \text{water}\end{cases} \tag{1}$$

where $\overline{Vo_a}$ and $\overline{Vo_w}$ are the averaged voltages for air and water phase respectively. On the other hand, the image processing of EBDT is a combination of several existing and new algorithms.

3.2. Image-processing method

The implementation of the EBDT included three steps: (1) pre-processing, (2) bubble segmentation and (3) free-surface detection. The first two steps were performed using the open source package ImageJ (Abràmoff et al., 2004). The original ultra-high-speed images were 8-bit greyscale pictures (Fig. 3a). The pre-processing aimed to minimise the noise from camera sensor, the non-uniform illumination and the out-of-focus bubbles. The sensor produced the salt-and-pepper noise, which was removed by the median filter while preserving the edge sharpness of the image. The non-uniform illumination was induced by the large variation in void fraction distributions in the roller, and its noise was removed by subtracting a Gaussian blurred image from the original one. The "rolling ball" algorithm (Sternberg, 1983) was used to reduce the background information. The result of pre-processing is shown in Fig. 3b. For the bubble segmentation, the pre-processing image was binarised using the iterative selection method (Ridler et al., 1978). Note that several binarisation methods are implemented in ImageJ, and other methods generated salt-and-pepper noise for the breaking bore. The "Fill Hole" function was applied to further fill the enclosed outline arcs of bubbles.

The next step was the bubble segmentation. In this case, the breaking bore is a more complex flow than the gas–liquid flows listed in Table 2. The bubbles exhibited random shapes under strong turbulence, shearing and surface tension, and the high void fraction led to intensive bubble–bubble interactions, forming bubbly clouds. Therefore, the breakpoint technique could not be used for the bubble segmentation, since the breakpoint method would generate random boundaries to separate the bubbles with random shape, and the separation of individual bubble was achieved by the watershed method (Fig. 3c). The bore free surface was detected in each frame using the technique presented by Wüthrich et al. (2020). The final output of the EBDT for a video frame is shown in Fig. 3d, where the white and black areas represent the air and water phases,respectively.

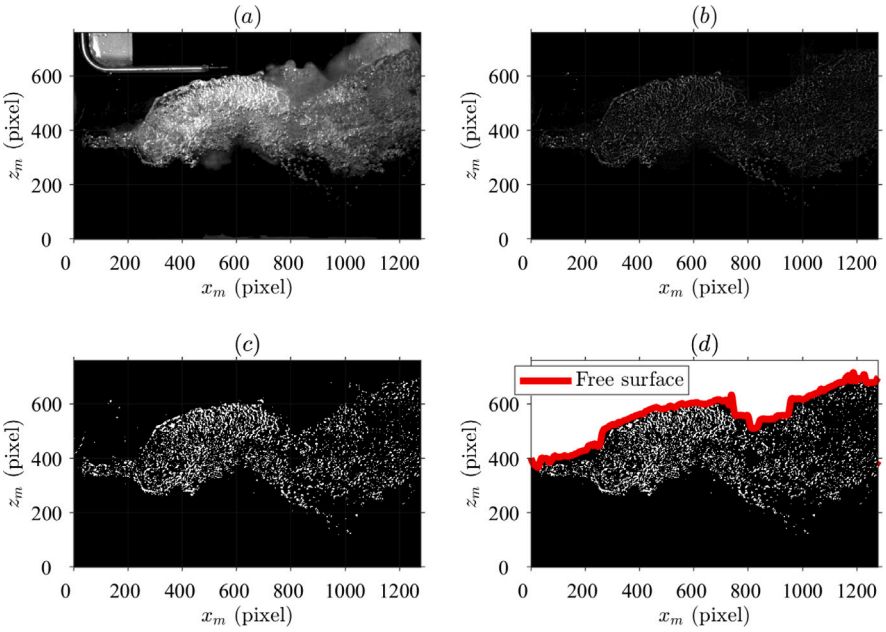

Fig. 3. Enclosed bubble detection technique (a) original 8-bit greyscale image (b) new image after pre-processing (c) image after binarisation and bubble segmentation (d) final output, with free surface plotted as a reference. Bore propagation from right to left.

The quantitative results of the above method were affected by the rolling ball radius and the window size of the median filter. These two parameters were selected based on a sensitivity study in a rectangular bubbly column with controlled void fraction (Appendix A). Overall, the results in the bubbly column suggested that the rolling ball radius of 5 pixels and window size of 2 by 2 pixels provided the smallest error range (1.2–5.2%), for void fraction between 0.026% to 0.216%. Fig. 4 presents the edge detection of the post-processed bubbles, with the original image plotted as reference. From Fig. 4, the EBDT highlighted these in-focused bubbles with random shapes. Since there is a lack of knowledge to predict the local bubble shape in the bore, the bubble reconstruction was considered impossible. Herein, the bubble size was derived from the direct outputs of watershed method, which might result into under- and over-estimation.

3.3. Validation and discussion

The parameters used in EBDT were derived from a series of bubbly column tests (Appendix A). A further validation was done by comparing the instantaneous void fraction signal c_v from image processing with the instantaneous void fraction signal c_p of the sidewall probe. The c_v signal was taken as the mean value of a small window with 3 × 3 pixels, which was the same size of the phase-detection probe sensor tip. Fig. 5 presents two examples of comparison between the image-processing and probe signals, showing a good agreement with some local differences.

The differences between the two signals are discussed herein, with some illustration in Fig. 6. The image-based technique provided a much deeper transverse detection region (in-focus plane of 15 mm) than the phase-detection probe (sensor diameter of 0.25 mm). More bubbles tended to be detected by the camera, since some bubbles appeared between the probe tip and sidewall glass (Fig. 6a). Large bubbles in the EBDT signal c_v might be regarded as a cluster of several bubbles in the phase-detection probe signal c_p (Fig. 6b). Assuming the same bubble at a given time, the chord time of the c_v signal was usually larger than that in the c_p signal, since the two-dimensional image only captured the maximum bubble chord (Fig. 6c). Overall, the authors acknowledge the differences between image-based results and direct probe measurements.

4. Ensemble-averaged void fraction from image processing

The contour maps of instantaneous void fraction using EBDT were ensemble-averaged, based on 71,556 frames from 80 ultra-high-speed videos, denoted as C_{EA}. The implementation of a synchronisation technique e spatially shifted the data using the reference position of the roller toe, assuming that the breaking bore translated as quasi-steady flow (Shi et al., 2021a). The contour plot of the ensemble-averaged void fraction using EBDT is presented in Fig. 7a, with the bore propagating from right to left in the image plane. Large void fraction data were observed immediately downstream of the roller toe. With increasing distance $(x - x_{toe})/d_1$ from the roller toe, the void fraction decreased in the roller, because of the de-aeration by buoyancy. Near the surface region, layered contour lines were observed for $C_{EA} \geqslant 0.3$, and the characteristic free-surface profile might be defined as the contour of $C_{EA} = 0.5$. In addition, the ensemble-averaged void fraction was derived from an brightness based technique (BBT) previously applied in the breaking bore (Leng and Chanson, 2019b). Note that the BBT and EBDT were classified as the brightness thresholding and bubble recognition approaches respectively, which were discussed in Section 3.1. The BBT developed by Leng and Chanson (2019b) interpolated the void fraction using a calibrated function between void fraction and brightness intensity, and similar techniques were used in hydraulic jump (Mossa and Tolve, 1998; Leandro et al., 2012). The contour plot of BBT is shown in Fig. 7b. The comparison indicated a good agreement in the roller toe region and free-surface region. The BBT highlighted little air diffusion for $(x - x_{toe})/d_1 > 1$, while the EBDT results were more consistent with the observed bubble advection in the breaking roller.

Different analytical models were used to describe the air diffusion in the breaking roller. Immediately downstream of the roller toe, the entrained air pockets were mainly subjected to buoyancy, drag and gravitational forces. Thus, the conservation of air mass provided analytical solutions of void fraction as a function of a characteristic elevation, as presented in Table 3 and Appendix B. These air pockets started to interact with the turbulent structure in the breaking roller, breaking into finer pieces. Then, the roller could be divided into the recirculation region in the free-surface region and vortex advection layer (Chanson, 1995). In the recirculation region, the solution of the air diffusion followed an error function, while the advection-diffusion model was commonly used in the shear layer (Chanson, 1989). Overall,

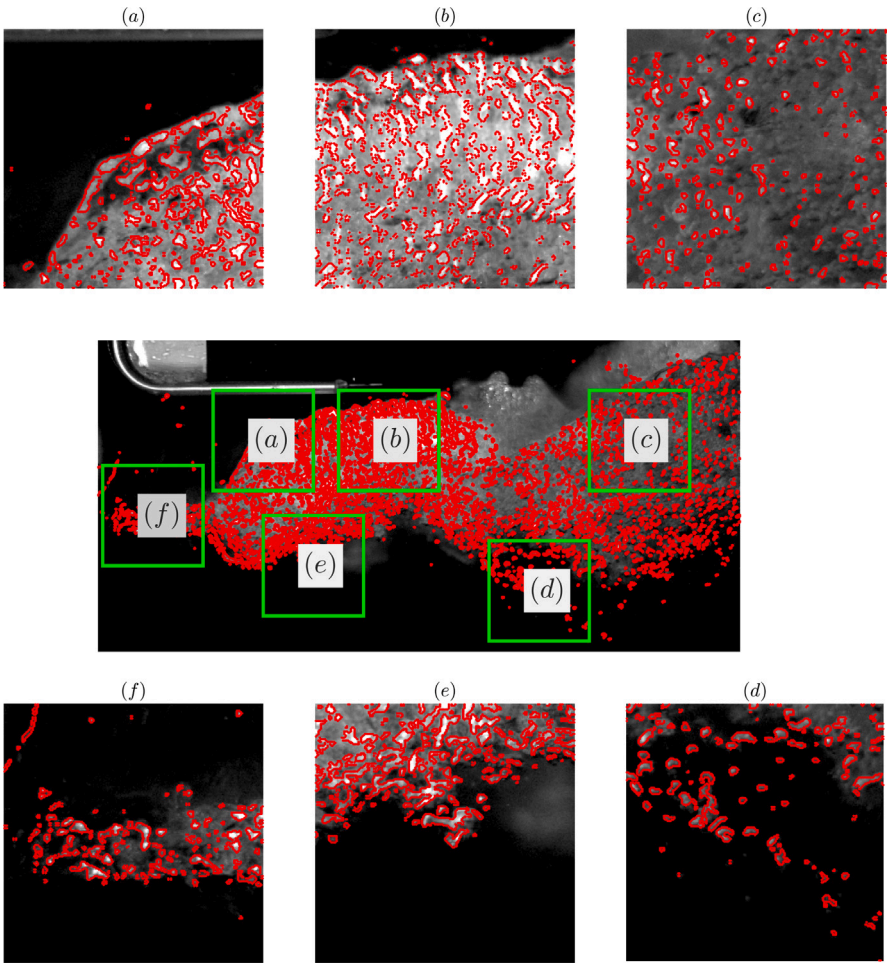

Fig. 4. Edge detection of post-processed bubbles with original image and zoomed-in subplots.

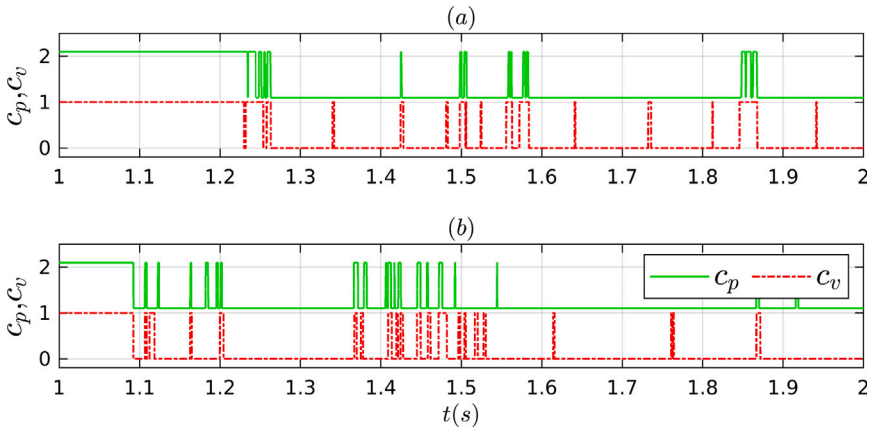

Fig. 5. Comparison of the binarised instantaneous void fraction signals using phase-detection probe c_p and EBDT signals c_v at $z/d_1 = 1.19$. Note that the probe signals were shifted upward for 1.1 units for a better visualisation.

Table 3 summarises on the different analytical models, which were compared with the void fraction profiles using EBDT in Fig. 8. The data showed that these analytical diffusion models were able to describe well the air-diffusion process.

The key properties of the void fraction profiles obtained using EBDT are presented in Fig. 9, namely the maximum void fraction in the shear layer, the corresponding vertical elevation, and the diffusivity coefficient. With increasing longitudinal distance from the roller toe, the maximum void fraction decreased in the shear layer, consistent with the advection-diffusion process. The vertical elevation of the maximum void fraction increased in the shear layer, indicating that the buoyancy caused an upward motion of the advected bubbly structures. The diffusivity coefficients $D^{\#}$ and D^{*}, obtained from the best-fit of the EBDT data, decreased and increased respectively further away from the roller toe, consistent with the previous data in hydraulic jumps in terms of order of magnitude and trend (Murzyn et al., 2005; Wang et al., 2015a). The diffusivity coefficients $D^{\#}$ and D^{*} were best-correlated as:

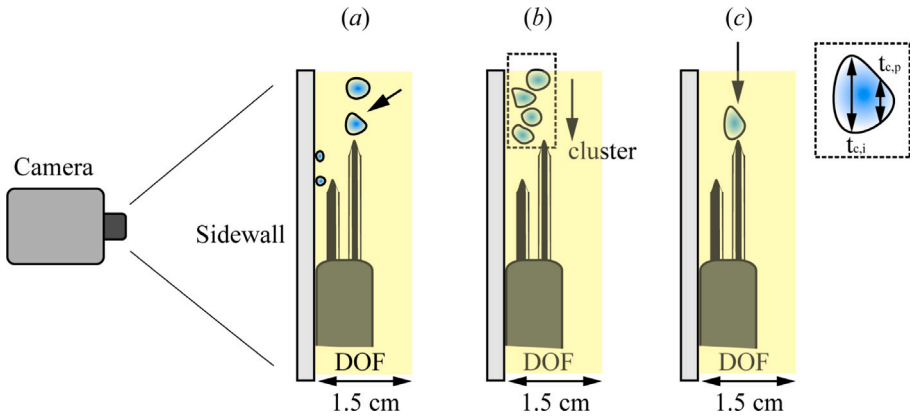

Fig. 6. Sketches of three cases of bubble motion next to channel sidewall, where $t_{c,i}$ and $t_{c,p}$ are the bubble chord time measured using image-based technique and phase-detection probe. Arrow indicating the bubbly flow direction.

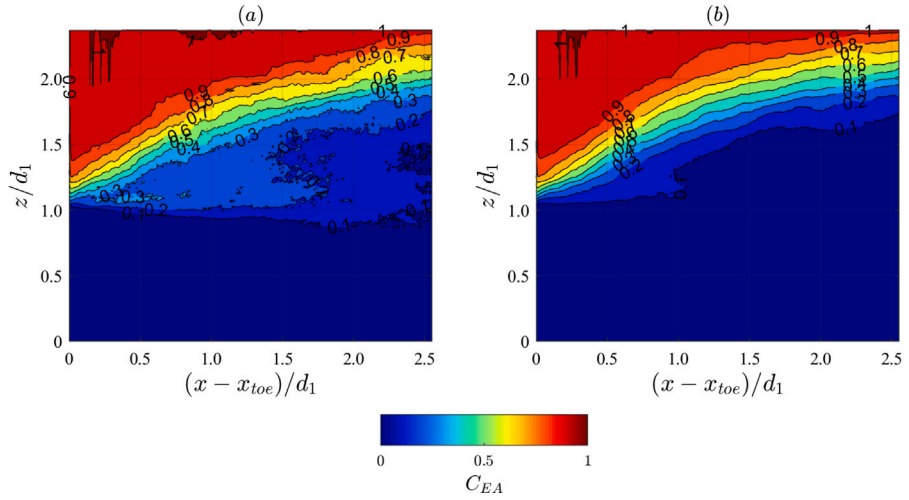

Fig. 7. Contour plots of ensemble-averaged void fraction C_{EA} for (a) EBDT (b) brightness thresholding technique (BBT) of Leng and Chanson (2019b), with bore propagation from right to left, and $Fr_1 = 2.4$, $Re = 2.3 \times 10^5$.

Table 3
Analytical solutions of air diffusion in breaking roller.

Region 1: immediate downstream of roller toe:		
$C_{EA} = 0.9\left(\frac{z - d_1}{z_{90} - d_1}\right)^N \quad 0 < z < z_{90}$	(2)	Present study (App. B)
Region 2: recirculation zone near the free surface		
$C_{EA} = \frac{1}{2}\left[1 + \text{erf}\left(\frac{z - z_{50}}{2\sqrt{D^*(x_{toe} - x)/(V_1 + U)}}\right)\right] \quad z > z^*$	(3)	Chanson (1989)
Region 3: Advection-diffusion zone in developing shear layer		
$C_{EA} = C_{EA,max}\exp\left[-\frac{1}{4D^\#}\frac{(z - Z_{Cmax})^2}{d_1(x_{toe} - x)}\right] \quad 0 < z < z^*$	(4)	Chanson (1995)

Notes: $C_{EA,max}$ the local maximum ensemble-averaged void fraction in the shear layer, and its corresponding vertical location Z_{Cmax}; z_{50} the vertical location of $C_{EA} = 0.5$; Z^* the vertical location for the boundary between the shear layer and recirculation zone; $D^\#$ and D^* diffusivity coefficients in the shear layer and recirculation zone, obtained from the best-fit.

$$D^* = 0.014\exp\left(-1.2\frac{x - x_{toe}}{d_1}\right) + 0.0025 \tag{5}$$

$$D^\# = 0.014\left(\frac{x - x_{toe}}{d_1}\right) + 0.0189 \tag{6}$$

5. Bubbly dynamics in breaking roller

5.1. Pseudo bubble count rate

A virtual phase-detection probe was introduced to compute a pseudo bubble count rate from the EBDT signal. Herein, the word "pseudo" meant that the control volume was relatively fixed at the same longitudinal distance from the roller toe during the bore propagation, based on the quasi-steady flow theory. The virtual probe was translated with the instantaneous bore celerity, thus providing a pseudo Lagrangian measurements at a location relative to the roller toe. Fig. 10 gives a detailed illustration on the virtual probes at two different time instants during the bore passage. The virtual probes in Fig. 10 measured the pseudo bubble count rate at the same longitudinal distance from the roller toe. Given the needle sensor size of the real phase-detection probe (0.8 mm), it was equivalent to take a mall neighbourhood region with 3-by-3 pixels in the image plane from the binarised video signals. The instantaneous void fraction for each frame was estimated as the mean value of the 3-by-3 pixel region. Then, an instantaneous void fraction signal was obtained over all the frames of an ultrahigh-speed video for a small neighbourhood region. The single threshold technique (Eq. (1)) was applied to identify the bubble chord time in the signal for a video, thus deriving the total number of bubbles f_i over a duration of T_i. The pseudo bubble count rate was defined as:

$$F_i = \sum_{i=n} f_i / \sum_{i=n} T_i \tag{7}$$

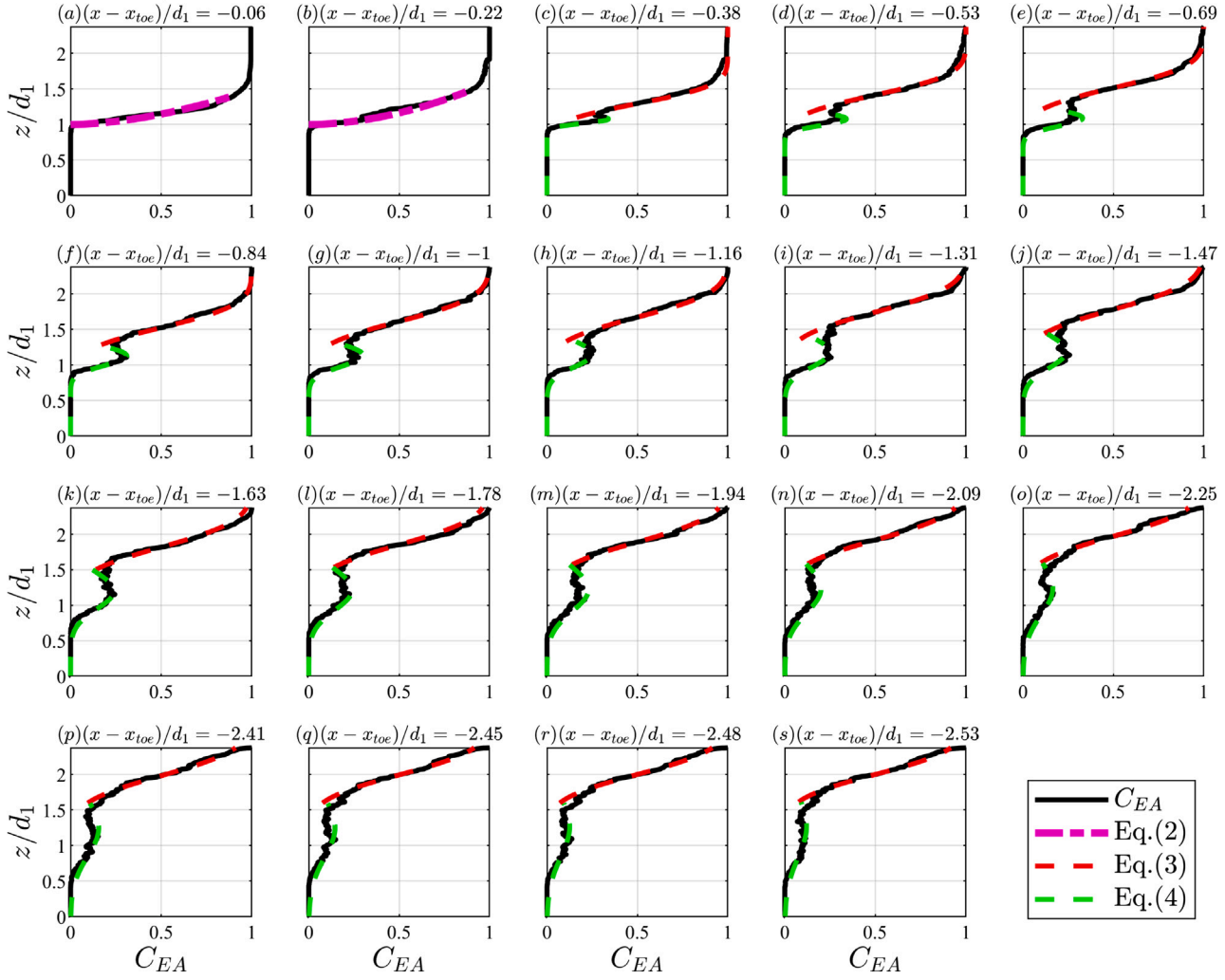

Fig. 8. A comparison between the vertical profiles of void fraction using EBDT and solutions of the different analytical solutions of air diffusion in breaking roller.

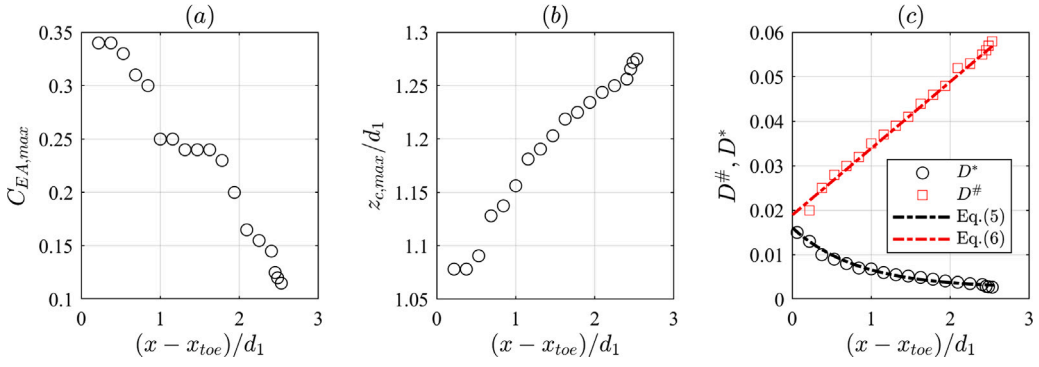

Fig. 9. Properties of void fraction profiles using EBDT as a function of dimensionless longitudinal distance in breaking bore (a) maximum void fraction in shear layer as a function of longitudinal distance (b) vertical locations of the maximum void fraction in shear layer as a function of longitudinal distance (c) diffusivity coefficients.

where n is the total number of videos. The present pseudo bubble count rate data were based on 80 videos with a total of 71,556 frames (7.16 s, based on 10,000 fps).

Fig. 11a presents the vertical profiles of the pseudo bubble count rate at several longitudinal locations from the roller toe, with the elevation z_{50} of $C_EA = 0.5$ as the characteristic free surface. The data exhibited a maximum value of bubble count rate $F_{1,max}$ in the developing shear layer, and a flattening vertical profile downstream of the roller toe. Physically, the high turbulent shear stress in the developing shear layer induced intense bubble-turbulence interplay, breaking bubbles into finer pieces. The vortex shedding occurred while bubbly coherent structures were advected downstream (Mortazavi et al., 2016), causing a decay in the ratio of inertial to buoyancy forces from the roller toe (Sene et al., 1994). During this process, some bubbles escaped from the coherent structures with possible occurrence of coalescence, corresponding to some decrease in maximum bubble

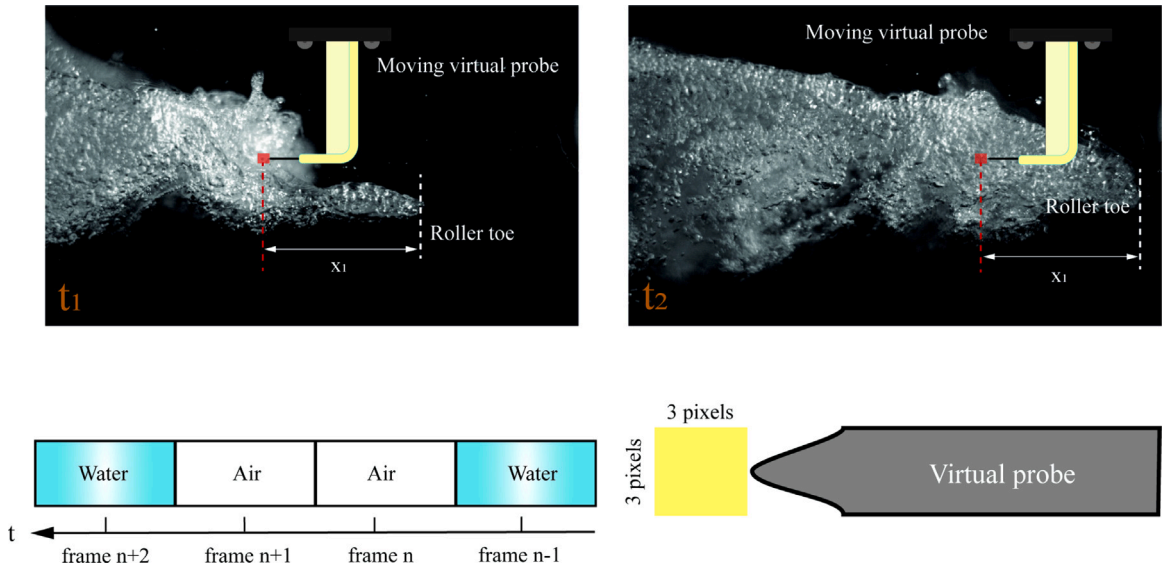

Fig. 10. Definition sketch of the virtual phase-detection probe at two different time instants during the bore passage.

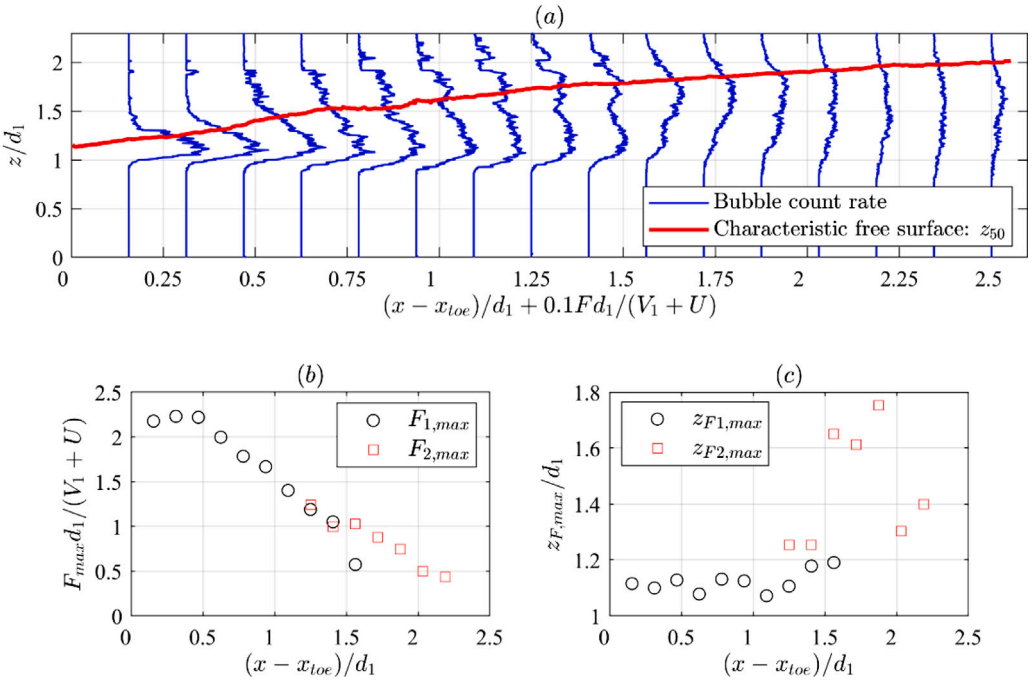

Fig. 11. Pseudo bubble count rate using EBDT (a) vertical profile at various longitudinal locations (b) maximum bubble count rate as a function of longitudinal distance (c) vertical locations of the maximum bubble count rate as a function of longitudinal distance.

count rate in the developing shear layer away from the roller toe (Fig. 11b). The buoyancy drove the escaped bubbles upwards, and the highly fluctuating free surface entrapped some bubbles, altogether resulting into the secondary peak of the bubble count rate $F_{2,max}$ in the recirculation zone from $(x - x_{toe})/d_1 \approx 0.9$. The secondary peak became larger than the primary peak $F_{1,max}$ for $(x - x_{toe})/d_1 > 1.5$, corresponding to the weakening the turbulent structures to let more bubbles escape from them. For completeness, Fig. 11c presents the vertical location of the maximum bubble count rate ($z_{F1,max}$ and $z_{F2,max}$) as a function of longitudinal distance. The $z_{F1,max}$ tended to be fairly constant, while $z_{F2,max}$ data were scattered. For $(x - x_{toe})/d_1 > 2.0$, the profiles exhibited a flat C-shape with the disappearance of both peaks.

5.2. Bubble size spectrum

The EBDT detected a large amount of bubbles while processing the videos (Figs. 3 and 4). However, the non-regular bubble shape made a direct measurement on bubble size near impossible. Thus, the concept of equivalent radius r was calculated as $r = \sqrt{A_r/\pi}$, where A_r is the bubble area, obtained from an automatic detection algorithm after the bubble separation from EBDT. The algorithm first detected the bubble locations from the binarised image, and counted the number of pixels occupied for a bubble. The bubble area A_r was derived from the sum of these pixels. Note that the algorithm required a large amount of computational power for processing all the high-speed videos in the present study.

The equivalent radius r ranged from $r = 0.2$ mm (approximately 1 pixel) to 15 mm, and the bubble size distribution is presented in Fig. 12.

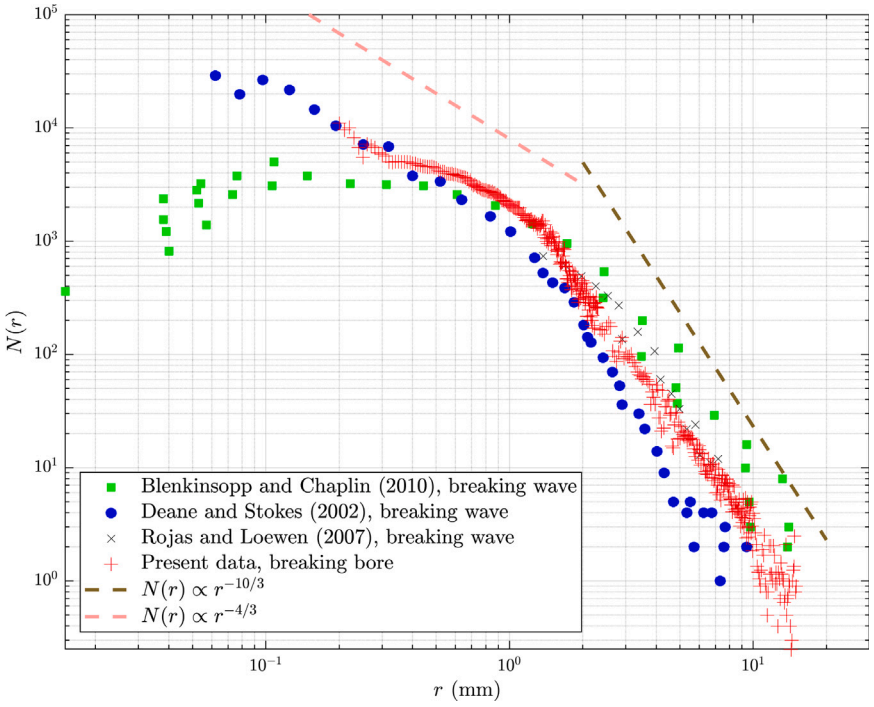

Fig. 12. Bubble size distribution N_r derived from the EBDT, in comparison to the distributions in breaking waves by Deane and Stokes (2002), Rojas and Loewen (2007) and Blenkinsopp and Chaplin (2010). Note that the previous data were obtained from the figure of Deike et al. (2016), and that the present number of bubbles was scaled down for a better comparison.

The bubble size distributions of Deane and Stokes (2002), Rojas and Loewen (2007) and Blenkinsopp and Chaplin (2010) in breaking waves are plotted for comparison in Fig. 12. Overall, the present bubble size distribution could be regarded as two regimes about the characteristic bubble size of $r = 2$ mm, based on the different data trends. Namely, in the regime of $r > 2$, the data exhibited a steeper slope than the data in regime of $r < 2$ mm, which were both described by the power law of radius $N(r) \propto r^{-m}$ (Garrett et al., 2000). For $r > 2$ mm, the present data agreed well with the data of Rojas and Loewen (2007), and were located between those of Rojas and Loewen (2007) and Blenkinsopp and Chaplin (2010). $m \approx 10/3$ for $r > 2$ mm was consistent with the findings of Deane and Stokes (2002), indicating that these large bubbles experienced a cascade break-up process in the inertia subrange (Garrett et al., 2000). The cascade ended at the Hinze scale, beyond which the bubbles could not be further broken down by turbulence because of the surface tension. For the present bore, the Hinze scale might be close to the bubble size of $r = 2$ mm. The bubbles smaller than the Hinze scale exhibited a different bubble break-up mechanism. Thus, the bubble size distribution of $r < 2$ mm was more comparable with that of Deane and Stokes (2002), with $m \approx 4/3$.

5.3. Bubble clustering

The phase-detection probe provided Eulerian measurements of bubble size in the streamwise direction in the roller. The longitudinal bubble chord time was directly obtained from the instantaneous void fraction signal of the phase-detection probes, and was used to investigate the non-random particle grouping in the shear layer, namely bubble clustering (Tooby et al., 1977; Sene et al., 1994). The near-wake criterion defined the clustering events (Chanson et al., 2006; Wang et al., 2015a). This is, two bubbles that travelled in the streamwise direction formed a cluster when the chord time of the leading bubble was greater than the separation water chord time between the two bubbles. The bubble clustering was characterised by its cluster count rate defined as the average number of clusters per run F_{clu}, the cluster size N_{clu} defined as the average numbers of bubble per cluster, and the cluster proportion P_{clu} defined as the ratio of the bubbles in cluster to the total number of bubbles.

Fig. 13 presents these bubble clustering properties, which were ensemble-averaged over 100 repetitions at a given location. The cluster count rate data ranged from 0 to 5 Hz, with the primary peak located at $z/d_1 = 1.5$. In the free-surface region, a secondary peak of the cluster count rate might not truly represent the clusters induced by the large-scale turbulent structures. It was likely caused by the free-surface fluctuations, exposing the probe tip into air. The cluster size and cluster proportion distributions exhibited similar trends, showing a primary peak at the same elevation of the cluster count rate data. On the other hand, a good agreement was observed between the sidewall and centreline data. At a given location, the high cluster count rate might indicate the presence of coherent structures with high frequency. The cluster size and cluster proportion might be proportional to the vorticity level. This is, the high centrifugal pressure gradient trapped more bubbles in the vortex core, and enhanced bubble-turbulence and bubble–bubble interplay (Sene et al., 1994). Three clustering properties exhibited a peak at $z/d_1 = 1.5$, possibly corresponding to the highest level of bubble-turbulence and bubble–bubble interplays in the bore roller. Overall, the clustering properties suggested that the bubbles did not randomly distribute in the breaking roller. Additionally, the clustering data were compared well with the data of Leng and Chanson (2019b), in terms of magnitude.

6. Conclusion

A characterisation of air–water properties in a breaking bore for $Fr_1 = 2.4$ has been presented. The experiments, obtained using an array of three intrusive dual-tip phase-detection probes and a non-intrusive ultra-high-speed camera, allowed both spatial and temporal measurements of the instantaneous void fraction in the breaking roller. The bore generation was a highly repeatable process. A large amount of experimental data were collected, including 100 repetitions of probe recording at each elevation (20 in total) sampled instantaneously with the camera at 10,000 fps. A novel enclosed bubble detection technique

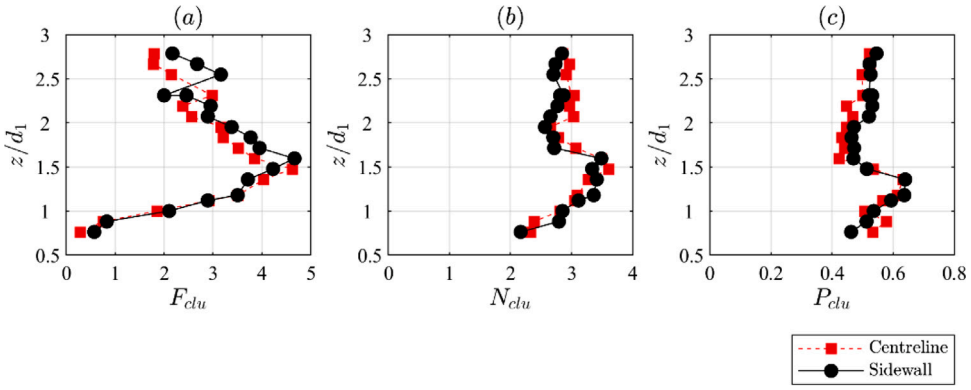

Fig. 13. Bubble clustering properties measured using phase-detection probe as a function of vertical distance: (a) average number of clusters per run F_{clu} (b) cluster size N_{clu} (c) cluster proportion P_{clu}.

(EBDT), synchronising the probe and camera, was developed to detect individual bubbles in the breaking roller, thus deriving detailed contour of void fraction and bubble properties. Overall, a number of concluding remarks have been drawn from the present work.

The EBDT was developed to specifically target the gas–liquid flow with relatively high void fraction (> 10%) compared to literature, where the intensive turbulence–bubble and bubble–bubble interactions could cause uncertainties for image processing. The selection of parameters in image processing played important roles for the result accuracy. The implementation of EBDT required a validation test, which was achieved by using rectangular bubbly column with controlled void fractions. Some errors were inevitable using general image-based techniques in gas–liquid flows. Hence, suitable filtering techniques may be considered with careful validation for the future use. The present work managed to minimise the error within 5%, which was reasonable for the gas–liquid flow with void fraction over 25%. Additionally, the void fraction data using EBDT outperformed the void fraction data using a brightness-based image-processing technique.

The dense void fraction distribution were obtained with a new level of details in the breaking bore roller. The ensemble-averaged void fraction was derived based on quasi-steady flow theory. In the roller toe region, assuming that the bubble motion had no impact of turbulence and subjecting to buoyancy, drag and weight, an analytical solution of void fraction as a function of vertical distance was derived. When the turbulent coherent structures formed, the air diffusion followed an error function in the free-surface region, and an advection diffusion model in the shear layer. These analytical solutions predicted the air diffusion in both hydraulic jump and breaking bore, suggesting that the bore and jump shared similar physical process in their roller.

The ensemble-averaged bubble clustering properties using phase-detection probe proved that the bubble grouping was a non-random process in the shear layer, as the bubbles were carried by the large-scale coherent structures. The pseudo bubble count rate was derived based on the quasi-steady flow theory, showing similar spatial distributions as those in stationary hydraulic jump. Furthermore, the bubble size was estimated using the equivalent radius r. The present bubble size spectrum followed the most commonly adopted model: $N(r) \propto r^{-m}$, and the change in gradient occurred at $r \approx 2$ mm, corresponding to the Hinze scale. For the bubbles with $r > 2$ mm, $m = 10/3$ indicating that the break-up mechanism was coupled with turbulence cascade in the inertia subrange. The good agreement between bubble size distributions in the breaking bore and breaking waves was observed.

CRediT authorship contribution statement

Rui Shi: Conceptualization, Methodology, Software, Formal analysis, Visualization, Writing – original draft. **Davide Wüthrich:** Conceptualization, Methodology, Software, Formal analysis, Visualization, Writing – original draft, Project administration. **Hubert Chanson:** Conceptualization, Methodology, Writing – review & editing, Supervision.

Declaration of competing interest

The authors declare the following financial interests/personal relationships which may be considered as potential competing interests: In line with recommendations of the Office of the Commonwealth Ombudsman (Australia) and International Committee on Publication Ethics (COPE), Hubert Chanson has a conflict of interest with Matthias Kramer (UNSW Canberra).

Data availability

Data will be made available on request.

Acknowledgements

The authors would like to thank Dr Hubert Branger (Aix Marseille Université, France), Dr Nobuhito Mori (Kyoto University, Japan), Dr Xinqian (Sophia) Leng (University of Bordeaux, France) and Professor Hang Wang (Sichuan University, China) for helpful suggestions and advice. The authors acknowledge the technical assistance of Jason Van Der Gevel and Stewart Matthrews (The University of Queensland, Australia). The financial support of the Swiss National Science Foundation (Grant P2ELP2_181794) and of the University of Queensland, School of Civil Engineering is acknowledged.

Appendix A. Bubbly column tests

A.1. Presentation

For the enclosed bubble detection technique (EBDT), the selection of key parameters was taken by conducting a series of new tests in a rectangular bubbly column with a wide range of void fraction. The bubbly column is commonly classified into homogeneous and heterogeneous regimes. In homogeneous regime, bubbles are uniformly distributed over cross-sectional, whereas heterogeneous regime is characterised by large-scale turbulence and a wide range of bubble sizes caused by bubble-turbulence interplay (Zahradnik et al., 1997). The heterogeneous flow is more similar to the turbulent flow in breaking bores, and was generated in the present bubbly column. There exists a large body of literature on rectangular bubbly columns, such as experimental investigations on void fraction (Magaud et al., 2001; Higuchi and Saito, 2010; Sasaki et al., 2017), and bubble dynamics (Lucas and Ziegenhein, 2019; Ziegenhein and Lucas, 2019; Liu et al., 2020), as well as CFD simulations (Tabib et al., 2008; Roghair et al., 2011; Ma et al., 2015). Since the present study focused on the two-phase properties in the breaking bore, no detailed review on bubbly column will be given unless necessary.

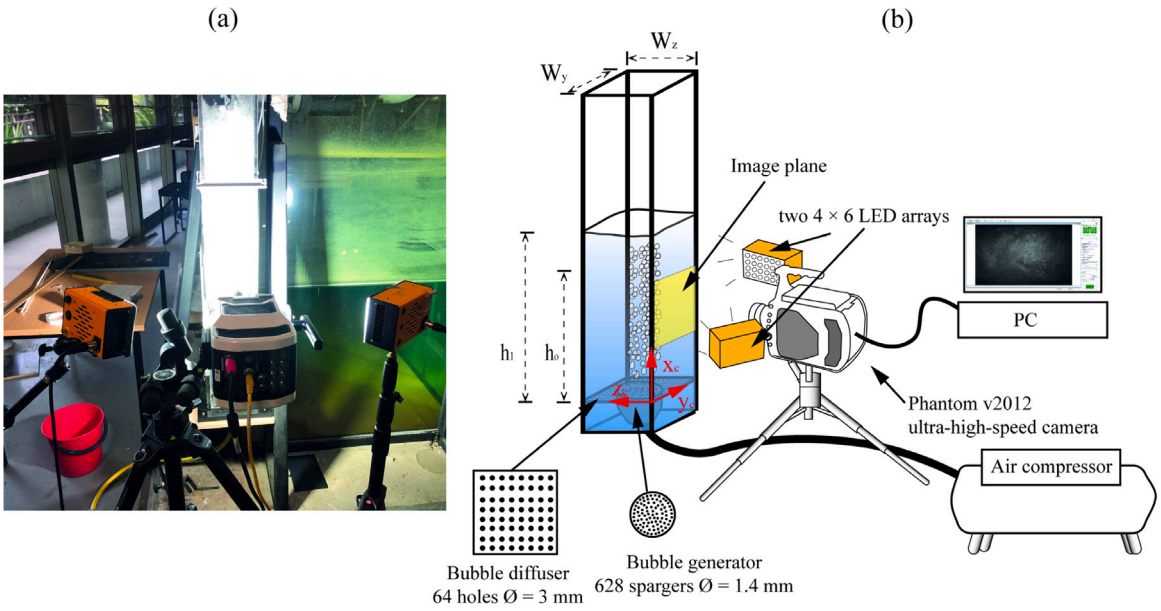

Fig. A.1. Experimental setup for the bubble column test: (a) photograph (b) a definition sketch.

A.2. Experimental facilities

The experiment setup consisted of a 1.2 m high rectangular column, an ultra-high-speed camera system, an air injection system, an air compressor and an illumination system (Fig. E-1). Zahradnik et al. (1997) suggested negligible effects of column diameter on the volume-averaged void fraction of heterogeneous bubbly flow when column diameter was equal and larger than 0.15 m, leading to the present column width and length of 0.15 m. The column was made of Perspex, with a height of 1.2 m. The column top remained open under atmospheric pressure, consistent with the breaking bore. The air was supplied from the air compressor (HD 300 LPM), and was issued to the bottom of column through a bubble generator, which had over 628 needle spargers. For needle sparger, a relative large diameter (1.4 mm) was used to achieve heterogeneous regime for any void fraction in the column (Ruzicka et al., 2001). A bubble diffuser, built with 64 large holes with a diameter of 3 mm, was placed on the top of the bubble generator, enhancing the bubble-turbulence interplay and mixing process. The coordinate system of the bubbly column is introduced in Fig. A.1: the streamwise coordinate x_c is positive upwards; the horizontal coordinate y_c is positive from the left to right of the image plane z_c is the transverse coordinate. The initial water level (h_0) was located at $x_c = 0.8$ m above the bubble generator. The volume-averaged void fraction was defined as:

$$\overline{C_c} = \frac{h_1 - h_0}{h_1} \tag{A.1}$$

where h_1 is the average water level of air–water flow. The flow condition in bubbly column was characterised by its volume-averaged void fraction $\overline{C_c}$. Six volume-averaged void fraction (0.026, 0.051, 0.085, 0.107, 0.176 and 0.223) were investigated in the present study. The camera set-up was same as that in breaking bore, except for two LED arrays angled 45°from both sides of the camera (Fig. A.1). The image plane covered the entire column width, with its centre at $x_c = 0.5$ m, not capturing the free-surface fluctuations and bubble diffuser. The duration of ultra-high-speed videos was 9.93 s, with a full HD resolution of 1280 × 800 pixels and sampling rate of 5000 fps.

A.3. Sensitivity analysis

A sensitivity analysis was conducted to select the two key parameters in the EBDT, including the rolling ball radius (R_b) and the median filter size for pre-processing (M_p). Note that the rolling ball algorithm with $R_b > 20$ contained large background noise in this case, thus leading to the selection of five radiuses (R_b = 1, 3, 5, 10, 15 and 20) in the sensitivity analysis. A median filter size larger than 4 × 4 pixels tended to blur the video image from the original image. Therefore, four sizes (M_p = 1×1, 2 × 2, 3×3 and 4 × 4) were tested for median filter. The sensitivity analysis covered all combinations from the two parameters (24 cases) for each void fraction. Since the sensitivity analysis generated massive data, only a summary on error

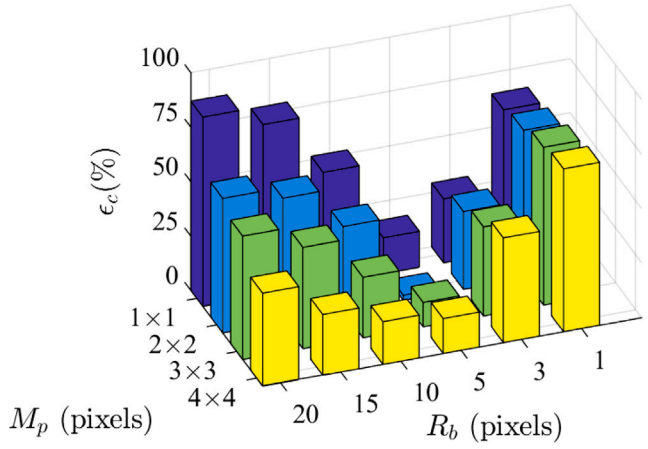

Fig. A.2. Error distributions of sensitivity analysis on rolling ball radius and median filter size for $\overline{C_c} = 0.223$.

Table A.4
Summary of error study in bubbly column.

$\overline{C_c}$	R_b	M_p	$\overline{C_i}$	$(\overline{\epsilon_c})_{min}$
0.026	10	3 × 3	0.022	3.4%
0.051	5	2 × 2	0.050	2.1%
0.085	5	2 × 2	0.082	3.8%
0.107	5	2 × 2	0.101	5.2%
0.176	5	2 × 2	0.178	1.2%
0.223	5	2 × 2	0.216	3.4%

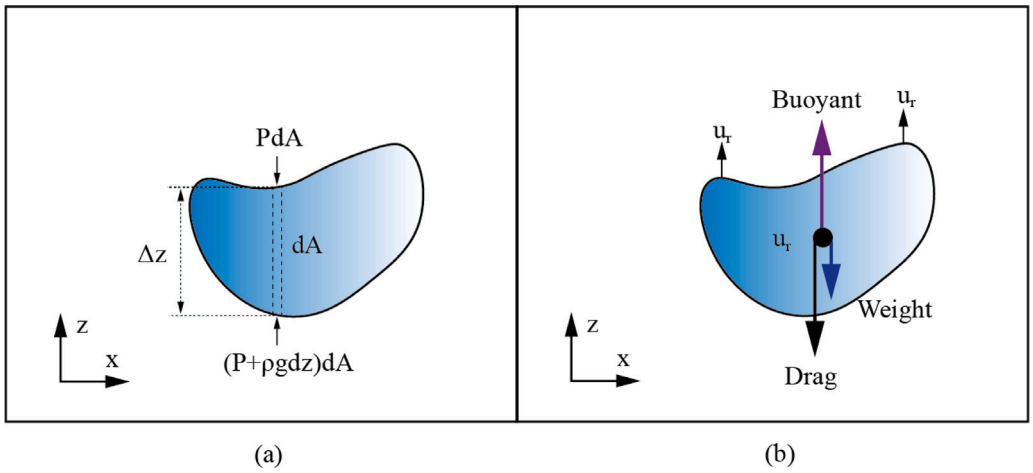

Fig. B.3. Forces acting on a submerged bubble rising in a liquid (a) Pressure forces acting on submerged bubble; (b) Forces acting on a bubble rising with a terminal rise velocity.

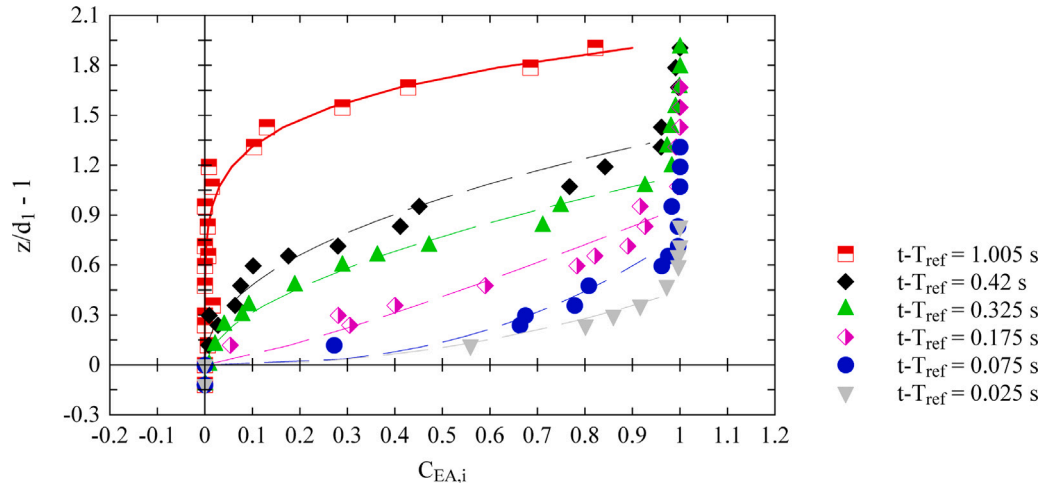

Fig. B.4. Vertical distributions of ensemble-averaged instantaneous void fraction in the leading edge of present breaking bore $Fr_1 = 2.4$.

is presented here. For each case, the mean value $\overline{C_i}$ of time-averaged void fraction distribution was calculated from entire image plane. The error was defined as:

$$\overline{\varepsilon_c} = \frac{\overline{C_c} - \overline{C_i}}{\overline{C_i}} 100\% \tag{A.2}$$

Fig. A.2 presents an example of error results for $\overline{C_c} = 0.223$, showing that the combination of $R_b = 5$ and $M_p = 2 \times 2$ provided the smallest error $(\overline{\varepsilon_c})_{min} = 2.33\%$. An summary of error study for the six void fractions is presented in Table A.4. Overall, the case of $R_b = 5$ and $M_p = 2 \times 2$ was able to provide the smallest error, except for the void fraction $\overline{C_c} = 0.026$. For the low void fraction, the bubble overlapping was less severe, thus the more out-of-focus information required "heavier" filtering achieved by large R_b and M_p values. In the breaking bore, the void fraction was unlikely to be less than 5%, thus $R_b = 5$ and $M_p = 2$ were used in the present study.

It is acknowledged that several factors could induce some errors: (1) non-uniformed bubble distributions in the heterogeneous regime of bubbly flow led to different void fraction of the image plane from the volume-averaged void fraction; (2) adopted parameters in EBDT over filtered the image data; (3) advection of bubbly flow structures induced local non-uniform illumination (reflection), biasing the binarisation process in EBDT.

Appendix B. Air diffusion model

B.1. Derivation

In an advancing breaking roller, the initial flow region in front of the bore is typically non-aerated. With the passage of the bore front, strong interfacial aeration and de-aeration take place through the upper surface of the roller, with surface breaking and uncontrolled air exchanges. The turbulent diffusion of air into the roller must counterbalance the detrainment induced by buoyancy effects. For a small control volume within the roller, the equation of conservation of mass for air in the air–water flow gives (Chanson, 1996):

$$\frac{\partial}{\partial z}\left(D_t \frac{\partial C}{\partial z}\right) = \frac{\partial}{\partial z}\left(C u_t\right) \tag{B.1}$$

where C is the void fraction, D_r is the turbulent diffusivity of air, u_t is the rise velocity of a bubble in air–water mixture.

The buoyant force on an air bubble in a fluid is the difference between the vertical components of the pressure force on its underside and on its upper side (Fig. B.3). For a single bubble rising at a constant velocity in a quiescent surrounding fluid, the drag and weight forces counterbalances the buoyant force:

$$\frac{1}{2} C_d \rho u_r^2 A_b + \rho_a g v_b = (\rho_w (1 - C) + \rho_a C) g v_b \tag{B.2}$$

with A_b the bubble projected area, C_d drag coefficient of bubble rising in air–water mixture, v_b the bubble volume, ρ the relevant fluid density, ρ_a air density, ρ_w water density. The rise velocity is:

$$u_r^2 = \frac{2gv_b}{C_d A_b} \frac{(\rho_w - \rho_a)(1-C)}{\rho} \tag{B.3}$$

considering the terminal bubble rise velocity in the clear water, the bubble rise velocity $(u_r)_{CW}$ equals:

$$(u_r)_{CW}^2 = \frac{2gv_b}{(C_d)_{CW}\rho_w A_b}\left(1 - \frac{\rho_a}{\rho_w}\right) \tag{B.4}$$

with $(C_d)_{CW}$ drag coefficient of bubble rising in clear-water. The ratio of terminal bubble rise velocity in air–water mixture to terminal rise velocity in clear water is expressed as"

$$\frac{u_r^2}{(u_r)_{CW}^2} = \frac{\rho_w (C_d)_{CW}}{\rho C_d}(1-C) \tag{B.5}$$

Replacing into Eq. (B.1), the equation of conservation of mass for air in the air–water flow becomes in dimensionless form:

$$D' \frac{\partial C}{\partial z'} = C\sqrt{\frac{\rho_w (C_d)_{CW}(1-C)}{\rho C_d}}, \text{ for } 0 < z' < 1 \tag{B.6}$$

with:

$$D' = \frac{D_t}{(u_r)_{CW}(z_{90} - d_1)} \text{ and } z' = \frac{z - d_1}{z_{90} - d_1} \tag{B.7}$$

z_{90} is the vertical location where void fraction is 90%, and it is commonly used to represent the free surface for highly fluctuated gravitational flow. Consider that zero diffusivity occurs as $C = 0$ & 1 and $\rho_w (C_d)_{CW}/\rho C_d \approx 1$, and that dimensionless diffusivity is:

$$D' = \frac{1}{N}\sqrt{1-C}\left(\frac{C}{0.9}\right)^{1/N} \tag{B.8}$$

the integration of the equation of mass for yields:

$$C = 0.9 z'^N \tag{B.9}$$

where N is positive, and related to the depth-averaged void fraction C_{mean} in the roller:

$$C_{mean} = \frac{1}{z_{90} - d_1}\int_{z=d_1}^{z_{90}} C\,dz \tag{B.10}$$

For $N < 1$, the vertical distribution of void fraction presents a convex profile for $0 < (z - d_1)/(z_{90} - d_1) < 1$. For $N > 1$, a concave shape is observed. Note that, z' can be also scaled as $(z - d_1)/d_1$.

B.2. Validation

The void fraction model derived above is a function of the vertical elevation. The validation was done using the intrusive void fraction measurements from the centreline probe. For experimental run, the bore arrive time T_{ref} was defined from the reference probe. Based on T_{ref}, the ensemble-averaged time-series of instantaneous void fraction $C_{EA,i}$ were obtained from 100 runs at a given location. Fig. B.4 presents several $C_{EA,i}$ profiles at different time, which agree well with the analytical solutions (curves). The analytical model was further tested and validated against unsteady void fraction data in dam break waves. In a dam break wave on a dry chute, the void fraction data (Chanson, 2004) showed a time-evolution of the vertical profiles from a convex to a concave shape. Eq. (B.9) was found to provide a good agreement with vertical profiles of instantaneous void fraction in dam break waves as well as in the leading edge of breaking roller (Shi et al., 2021b)

The present development is based upon a number of basic assumptions. First, the flow is assumed to be quasi-steady and the analysis is performed in the system of references in translation with the bore roller toe. Second, the bore roller is quasi-steady, i.e. it does not change with time. Third, self-aeration is predominantly an interfacial process, only driven by buoyancy, i.e, bubble turbulence and bubble-turbulence interactions are predominantly once shear layer forms. Therefore, the model was considered valid either near the roller toe, where large bubble pocket are not yet broken down by turbulence, or further downstream, where individual bubbles were separated from bubble flows.

References

Abràmoff, M.D., Magalhães, P.J., Ram, S.J., 2004. Image processing with ImageJ. Biophoton. Int. 11 (7), 36–42.

Blenkinsopp, C., Chaplin, J., 2007. Void fraction measurements in breaking waves. Proc. R. Soc. A 463 (2088), 3151–3170.

Blenkinsopp, C.E., Chaplin, J.R., 2010. Bubble size measurements in breaking waves using optical fiber phase detection probes. IEEE J. Ocean. Eng. 35 (2), 388–401.

Brocchini, M., Peregrine, D., 2001. The dynamics of strong turbulence at free surfaces. Part 1. Description. J. Fluid Mech. 449, 225–254.

Bröder, D., Sommerfeld, M., 2007. Planar shadow image velocimetry for the analysis of the hydrodynamics in bubbly flows. Meas. Sci. Technol. 18 (8), 2513.

Bullock, G., Crawford, A., Hewson, P., Walkden, M., Bird, P., 2001. The influence of air and scale on wave impact pressures. Coast. Eng. 42 (4), 291–312.

Cartellier, A., Achard, J., 1991. Local phase detection probes in fluid/fluid two-phase flows. Rev. Sci. Instrum. 62 (2), 279–303.

Cerqueira, R.F., Paladino, E.E., 2021. Development of a deep learning-based image processing technique for bubble pattern recognition and shape reconstruction in dense bubbly flows. Chem. Eng. Sci. 230, 116163.

Chalgeri, V.S., Jeong, J.H., 2019. Flow regime identification and classification based on void fraction and differential pressure of vertical two-phase flow in rectangular channel. Int. J. Heat Mass Transfer 132, 802–816.

Chanson, H., 1989. Study of air entrainment and aeration devices. J. Hydraul. Res. 27 (3), 301–319.

Chanson, H., 1995. Air entrainment in two-dimensional turbulent shear flows with partially developed inflow conditions. Int. J. Multiph. Flow. 21 (6), 1107–1121.

Chanson, H., 1996. Air Bubble Entrainment in Free-Surface Turbulent Shear Flows. Academic Press, London, UK.

Chanson, H., 2004. Unsteady air–water flow measurements in sudden open channel flows. Exp. Fluids 37 (6), 899–909.

Chanson, H., 2012. Tidal Bores, Aegir, Eagre, Mascaret, Pororoca: Theory and Observations. World Scientific, Singapore.

Chanson, H., Aoki, S., Hoque, A., 2006. Bubble entrainment and dispersion in plunging jet flows: Freshwater vs. seawater. J. Coast. Res. 22 (3), 664–677.

Cox, D.T., Shin, S., 2003. Laboratory measurements of void fraction and turbulence in the bore region of surf zone waves. J. Eng. Mech. 129 (10), 1197–1205.

Deane, G.B., Stokes, M.D., 2002. Scale dependence of bubble creation mechanisms in breaking waves. Nature 418 (6900), 839–844.

Deike, L., Melville, W.K., Popinet, S., 2016. Air entrainment and bubble statistics in breaking waves. J. Fluid Mech. 801, 91–129.

Fu, Y., Liu, Y., 2016a. Development of a robust image processing technique for bubbly flow measurement in a narrow rectangular channel. Int. J. Multiph. Flow. 84, 217–228.

Fu, Y., Liu, Y., 2016b. Experimental study of bubbly flow using image processing techniques. Nucl. Eng. Des. 310, 570–579.

Gabriel, S., Schulenberg, T., Albrecht, G., Heiler, W., Miassoedov, A., Kaiser, F., Wetzel, T., 2018. Optical void measurement method for stratified wavy two phase flows. Exp. Therm Fluid Sci. 97, 341–350.

Garrett, C., Li, M., Farmer, D., 2000. The connection between bubble size spectra and energy dissipation rates in the upper ocean. J. Phys. Oceanogr. 30 (9), 2163–2171.

Higuchi, M., Saito, T., 2010. Quantitative characterizations of long-period fluctuations in a large-diameter bubble column based on point-wise void fraction measurements. Chem. Eng. J. 160 (1), 284–292.

Honkanen, M., Saarenrinne, P., Stoor, T., Niinimäki, J., 2005. Recognition of highly overlapping ellipse-like bubble images. Meas. Sci. Technol. 16 (9), 1760.

Hoque, A., Aoki, S.-i., 2005. Distributions of void fraction under breaking waves in the surf zone. Ocean Eng. 32 (14–15), 1829–1840.

Kong, R., Rau, A., Kim, S., Bajorek, S., Tien, K., Hoxie, C., 2019. A robust image analysis technique for the study of horizontal air-water plug flow. Exp. Therm Fluid Sci. 102, 245–260.

Lamarre, E., Melville, W., 1991. Air entrainment and dissipation in breaking waves. Nature 351 (6326), 469–472.

Lamarre, E., Melville, W.K., 1994. Void-fraction measurements and sound-speed fields in bubble plumes generated by breaking waves. J. Acoust. Soc. Am. 95 (3), 1317–1328.

Lau, Y., Deen, N., Kuipers, J., 2013. Development of an image measurement technique for size distribution in dense bubbly flows. Chem. Eng. Sci. 94, 20–29.

Leandro, J., Carvalho, R., Chachereau, Y., Chanson, H., 2012. Estimating void fraction in a hydraulic jump by measurements of pixel intensity. Exp. Fluids 52 (5), 1307–1318.

Leng, X., Chanson, H., 2019a. Air-water interaction and characteristics in breaking bores. Int. J. Multiph. Flow. 120, 103101.

Leng, X., Chanson, H., 2019b. Two-phase flow measurements of an unsteady breaking bore. Exp. Fluids 60 (3), 1–15.
Lighthill, J., 1978. Waves in Fluids. Cambridge University Press.
Liu, Z., Li, X., Mao, Z.-S., Yuan, S., Yang, C., 2020. Hydrodynamics of gas phase in a shallow bubble column from in-line photography. Chem. Eng. Sci. 221, 115703.
Lucas, D., Ziegenhein, T., 2019. Influence of the bubble size distribution on the bubble column flow regime. Int. J. Multiph. Flow. 120, 103092.
Ma, T., Ziegenhein, T., Lucas, D., Krepper, E., Fröhlich, J., 2015. Euler–Euler large eddy simulations for dispersed turbulent bubbly flows. Int. J. Heat Fluid Flow 56, 51–59.
Magaud, F., Souhar, M., Wild, G., Boisson, N., 2001. Experimental study of bubble column hydrodynamics. Chem. Eng. Sci. 56 (15), 4597–4607.
Maurus, R., Ilchenko, V., Sattelmayer, T., 2002. Study of the bubble characteristics and the local void fraction in subcooled flow boiling using digital imaging and analysing techniques. Exp. Therm Fluid Sci. 26 (2), 147–155.
Merlivat, L., Memery, L., 1983. Gas exchange across an air-water interface: Experimental results and modeling of bubble contribution to transfer. J. Geophys. Res.: Oceans 88 (C1), 707–724.
Meyer, F., Beucher, S., 1990. Morphological segmentation. J. Vis. Commun. Image Represent. 1 (1), 21–46.
Mori, N., Kakuno, S., 2008. Aeration and bubble measurements of coastal breaking waves. Fluid Dyn. Res. 40 (7–8), 616.
Mortazavi, M., Le Chenadec, V., Moin, P., Mani, A., 2016. Direct numerical simulation of a turbulent hydraulic jump: Turbulence statistics and air entrainment. J. Fluid Mech. 797, 60–94.
Mossa, M., Tolve, U., 1998. Flow visualization in bubbly two-phase hydraulic jump. J. Fluid Eng. 120, 160–165.
Murzyn, F., Mouaze, D., Chaplin, J., 2005. Optical fibre probe measurements of bubbly flow in hydraulic jumps. Int. J. Multiph. Flow. 31 (1), 141–154.
Pei, S.-C., Horng, J.-H., 1995. Circular arc detection based on Hough transform. Pattern Recognit. Lett. 16 (6), 615–625.
Peregrine, D.H., 1983. Breaking waves on beaches. Annu. Rev. Fluid Mech. 15 (1), 149–178.
Poletaev, I., Tokarev, M.P., Pervunin, K.S., 2020. Bubble patterns recognition using neural networks: Application to the analysis of a two-phase bubbly jet. Int. J. Multiph. Flow. 126, 103194.
Rana, K., Agrawal, G., Mathur, J., Puli, U., 2014. Measurement of void fraction in flow boiling of ZnO–water nanofluids using image processing technique. Nucl. Eng. Des. 270, 217–226.
Rapp, R.J., Melville, W.K., 1990. Laboratory measurements of deep-water breaking waves. Philos. Trans. R. Soc. Lond. Ser. A 331 (1622), 735–800.
Ridler, T., Calvard, S., et al., 1978. Picture thresholding using an iterative selection method. IEEE Trans. Syst. Man Cybern. 8 (8), 630–632.
Rodríguez-Rodríguez, J., Marugán-Cruz, C., Aliseda, A., Lasheras, J.C., 2011. Dynamics of large turbulent structures in a steady breaker. Exp. Therm Fluid Sci. 35 (2), 301–310.
Roghair, I., Lau, Y., Deen, N., Slagter, H., Baltussen, M., Annaland, M.V.S., Kuipers, J., 2011. On the drag force of bubbles in bubble swarms at intermediate and high Reynolds numbers. Chem. Eng. Sci. 66 (14), 3204–3211.
Rojas, G., Loewen, M., 2007. Fiber-optic probe measurements of void fraction and bubble size distributions beneath breaking waves. Exp. Fluids 43 (6), 895–906.
Ruzicka, M., Zahradnık, J., Drahoš, J., Thomas, N., 2001. Homogeneous–heterogeneous regime transition in bubble columns. Chem. Eng. Sci. 56 (15), 4609–4626.
Sasaki, S., Uchida, K., Hayashi, K., Tomiyama, A., 2017. Effects of column diameter and liquid height on gas holdup in air-water bubble columns. Exp. Therm Fluid Sci. 82, 359–366.
Sene, K., Hunt, J., Thomas, N., 1994. The role of coherent structures in bubble transport by turbulent shear flows. J. Fluid Mech. 259, 219–240.
Shi, R., Leng, X., Chanson, H., 2021a. Breaking bore roller characteristics: Turbulence statistics using optical techniques. Coast. Eng. 168, 103893.
Shi, R., Wüthrich, D., Chanson, H., 2021b. Air-Water Characteristics of a Breaking Bore Roller Part II: Air-Water Flow Properties. Hydraulic Model Report CH118/20, The University of Queensland.
Shi, R., Wüthrich, D., Chanson, H., 2022. Air-water properties of unsteady breaking bores part 1: Novel Eulerian and Lagrangian velocity measurements using intrusive and non-intrusive techniques. Int. J. Multiph. Flow. 104338.
Stansby, P., Chegini, A., Barnes, T., 1998. The initial stages of dam-break flow. J. Fluid Mech. 374, 407–424.
Sternberg, S.R., 1983. Biomedical image processing. Computer 16 (01), 22–34.
Tabib, M.V., Roy, S.A., Joshi, J.B., 2008. CFD simulation of bubble column—An analysis of interphase forces and turbulence models. Chem. Eng. J. 139 (3), 589–614.
Teh, C.-H., Chin, R.T., 1989. On the detection of dominant points on digital curves. IEEE Trans. Pattern Anal. Mach. Intell. 11 (8), 859–872.
Tooby, P.F., Wick, G.L., Isaacs, J.D., 1977. The motion of a small sphere in a rotating velocity field: A possible mechanism for suspending particles in turbulence. J. Geophys. Res. 82 (15), 2096–2100.
Veron, F., 2015. Ocean spray. Annu. Rev. Fluid Mech. 47, 507–538.
Villegas, L.R., Colombet, D., Guiraud, P., Legendre, D., Cazin, S., Cockx, A., 2019. Image processing for the experimental investigation of dense dispersed flows: Application to bubbly flows. Int. J. Multiph. Flow. 111, 16–30.
Wang, H., Felder, S., Chanson, H., 2014. An experimental study of turbulent two-phase flow in hydraulic jumps and application of a triple decomposition technique. Exp. Fluids 55 (7), 1–18.
Wang, H., Hu, Z., Chanson, H., 2015a. Two-dimensional bubble clustering in hydraulic jumps. Exp. Therm Fluid Sci. 68, 711–721.
Wang, H., Murzyn, F., Chanson, H., 2015b. Interaction between free-surface, two-phase flow and total pressure in hydraulic jump. Exp. Therm Fluid Sci. 64, 30–41.
Witt, A., Gulliver, J., Shen, L., 2015. Simulating air entrainment and vortex dynamics in a hydraulic jump. Int. J. Multiph. Flow. 72, 165–180.
Wüthrich, D., Pfister, M., Nistor, I., Schleiss, A.J., 2018. Experimental study on the hydrodynamic impact of tsunami-like waves against impervious free-standing buildings. Coast. Eng. J. 60 (2), 180–199.
Wüthrich, D., Shi, R., Chanson, H., 2020. Physical study of the 3-dimensional characteristics and free-surface properties of a breaking roller in bores and surges. Exp. Therm Fluid Sci. 112, 109980.
Yu, X., Xing, D., Hazuku, T., Takamasa, T., Ishimaru, T., Tanaka, Y., Akiba, T., 2009. Measurement technique for solid-liquid two-phase flow using a normal-line Hough transform method. J. Phys.: Conf. Ser. 147 (1), 012053.
Zahradnik, J., Fialova, M., Ru, M., Drahos, J., Kastanek, F., Thomas, N., et al., 1997. Duality of the gas-liquid flow regimes in bubble column reactors. Chem. Eng. Sci. 52 (21–22), 3811–3826.
Ziegenhein, T., Lucas, D., 2019. The critical bubble diameter of the lift force in technical and environmental, buoyancy-driven bubbly flows. Int. J. Multiph. Flow. 116, 26–38.